Research Square

Preprints are preliminary reports that have not undergone peer review.
They should not be considered conclusive, used to inform clinical practice,
or referenced by the media as validated information.

Numerical Simulation Study on the Motion Behavior of WC Hard Phase Particles in the Laser Cladding Process of Nickel-Based WC60 Powder

Sen Wang
Chang Li
lichang2323-23@163.com

Chuang Wang
Chuanbin Ma
Wenping Xu
Xing Han

Research Article

Keywords: Laser cladding, Particle size effect, Multiphysics coupling, WC particles

Posted Date: August 13th, 2026

DOI: https://doi.org/10.21203/rs.3.rs-9826447/v1

License: This work is licensed under a Creative Commons Attribution 4.0 International License.
Read Full License

Additional Declarations: No competing interests reported.

Numerical Simulation Study on the Motion Behavior of WC Hard Phase Particles in the Laser Cladding Process of Nickel-Based WC60 Powder

Sen Wang[1], Chang Li[*1], Chuang Wang, Chuanbin Ma, Wenping Xu, Xing Han

(School of Mechanical Engineering and Automation, University of Science and Technology Liaoning, Liaoning Anshan, 114051, China)

[1] Sen Wang and Chang Li are co-first authors of the article.

* Correspondence: lichang2323-23@163.com, Tel.: 860412-5929771

Abstract:

The distribution uniformity of WC hard phase particles during laser cladding of Ni-based WC60 powder critically determines the mechanical properties and wear resistance of the coating. The frequent deposition of WC particles is a primary cause of coating cracking and performance degradation, with particle size playing a decisive role in this behavior. In this study, a 3D coupled thermal-flow-particle multiphysics model was established to investigate the motion and deposition of WC particles of five different diameters (144, 124, 104, 84, and 64 μm). The results show that coarse particles (124 and 144 μm) are inertia-dominated, moving along a slanting downward trajectory and finally concentrating at the bottom of the molten pool with high accumulation density. Fine particles (64 and 84 μm) are drag-dominated, horizontally transported to the pool edge by Marangoni convection, and dispersed over the upper, middle, lower and edge regions. Medium particles (104 μm) exhibit transitional behavior. The particle size effect can be quantitatively characterized by the Stokes number: as the particle size decreases, the deposition distribution gradually shifts from bottom-concentrated to edge-spread in a gradient manner. The predicted errors of the cladding layer height and width agree well with the experimental data; the simulated particle distribution trends are consistent with SEM observations. The proposed model effectively predicts the motion behavior of WC particles of different sizes, providing a theoretical basis for tailoring the spatial distribution of the reinforcing phase in laser cladding.

Keywords: Laser cladding； Particle size effect； Multiphysics coupling； WC particles

1 Introduction

Employing a high-energy laser beam to melt deposited powder on a substrate surface, laser cladding serves as an advanced technique for both surface reinforcement

and additive fabrication, yielding a metallurgically bonded layer characterized by superior wear and corrosion resistance. This technology finds extensive applications across sectors such as aerospace, petrochemical processing, and railway transportation. The WC-Ni metal matrix composite coating, due to its combination of the good toughness of nickel-based alloys and the high hardness of WC, is recognized as a high-performance coating, with excellent high-temperature resistance, corrosion protection, and wear resistance. Sun et al. provided a systematic assessment of how process parameters affect WC-Ni coating preparation via laser cladding. Their findings highlight that laser power, scanning speed, and powder feed rate substantially influence molten pool morphology and coating quality [1]. However, the different particle sizes of WC directly affect its movement behavior in the molten pool and the final spatial arrangement, thus determining the microstructure and the resultant macroscopic behavior of the coating.

In laser cladding of WC60-reinforced nickel-based coatings, the homogeneity of WC particle dispersion serves as a primary factor dictating overall coating performance.Research has demonstrated that WC particles preferentially settle toward the bottom of the molten pool, producing an inhomogeneous distribution of WC particles: the concentration of particles at the bottom is high, while that at the surface is low. Ortiz et al. established a distribution model of WC particles along the cross-sectional depth in the laser cladding of NiCrBSi + WC coating, and found that WC particles exhibit a tendency to accumulate at the bottom of the molten pool, with the percentage of WC at the bottom being higher than the theoretical set value while that at the top is lower than the theoretical value. This distribution model serves as a valuable reference for optimizing coating fabrication procedures [2]. Such non-uniform dispersion may induce stress concentration, trigger crack formation, and eventually cause coating delamination. Therefore, a deep understanding of the movement behavior of WC particles in the molten pool and the regulation of particle distribution have significant engineering significance.

Regarding the laser cladding of WC reinforced coatings, scholars from both domestic and international communities have conducted extensive research efforts. In terms of process parameter optimization, Weng and co-workers employed diode laser cladding for the fabrication of Ni/WC composite coatings, and found that through adjusting the laser power and adding 0.4wt% La, a composite coating spanning 20–60 wt% WC without cracking or porosity could be realized [3].Li et al. investigated the role of WC particle shape (spherical vs. non-spherical) in the microstructure and wear resistance of laser-clad Inconel 625, and the associated enhancement mechanisms for substrate wear/corrosion resistance [4]. In terms of powder feeding rate, it was found

that the feeding rate has a significant impact on the proportion by mass of WC particles, the evolution of the microstructure, and the microhardness.

Regarding the behavior and attributes of WC particles, scholars both at home and abroad have recognized that the content, size and morphology of WC particles critically determine the microstructure and final performance of the coating. Xu et al. studied the impact of WC particle content (0–80wt%) on the microstructure, microhardness and sliding wear performance of WC/Ni composite coatings fabricated by laser cladding, and found that the wear resistance of the WC/Ni composite coating strongly depends on the WC particle content and its microstructure [5]. Hu et al. applied high-speed laser cladding to produce Ni/WC composite coatings on 304 steel with various WC loadings. The prepared coatings demonstrated satisfactory surface formation, lacking any pores, cracks, or similar flaws, and featured a homogeneous dispersion of WC particles [6]. For WC particles of different sizes, Tan et al. systematically investigated the role of WC particle dimensions (30–65 μm, 65–100 μm and 100–145 μm) on both the microstructure and the tribological characteristics of Ni/WC composite coatings produced via high-speed laser cladding, and concluded that the particle size substantially influences the evolution of coating structure and wear resistance [7]. Zhang et al. demonstrated through the study on the laser cladding-based in-situ synthesis of WC-reinforced Ni-based cladding layers that the diameter and proportion of the cladding powder significantly affect the distribution of WC hard phase and the resultant cladding performance [8].

Regarding the thermal degradation behavior of WC particles, researchers have identified two forms of thermal damage and have deeply explored their effects on the microstructure evolution. Wang et al. systematically studied the thermal damage mechanism in WC particles within the laser-induced composite coating of Ni60/WC, and found that the main forms of thermal damage for WC particles were dissolution, diffusion, and slagification [9]. The findings indicated that as the laser cladding power increased, the decomposition of WC intensified, with the volume fraction decreasing from 41.6% to 30.2%. However, under low-stress wear conditions, the resistance to wear of the coating was proportional to the WC particle volume fraction. Regarding the matching of particle size and laser process parameters, the research established a speed model and a temperature rise model for enhancing particles, and clarified the critical size condition for ensuring the WC particles remain in a solid state: when the laser power density is 119W/mm², the particle size must be greater than 75μm; if WC particles with a diameter less than 75μm need to be injected, the laser power density must be reduced to below 95W/mm² [10].

In terms of particle movement regulation, ultrasonic impact treatment has been

proven to be able to alter the dispersion pattern of WC particles across the cladding layer. Studies have demonstrated that ultrasonic, through cavitation and acoustic flow, enhances convection in the molten pool, promoting the upward migration and homogeneous dispersion of WC particles deposited at the bottom; concurrently, it refines the grains and inhibits element segregation, improving the uniformity of the coating [11]. Additionally, electromagnetic field assistance has also been confirmed to affect the distribution behavior of WC particles, providing a new technical means for particle distribution regulation. Huo et al. demonstrated that electromagnetic composite field-assisted laser cladding enables even WC particle distribution, enhancing the microstructure by strengthening Marangoni convection, significantly improving the hardness of IN718/WC composite coating; the Ampere force generated by the electromagnetic composite field strengthens Marangoni convection within the molten pool, thereby enabling to a homogeneous dispersion of WC particles throughout the composite coating; nevertheless, overly vigorous Marangoni convection may cause WC particles to be expelled from the melt pool, with this effect being particularly pronounced for particles of small dimensions [12]. Figure 1 illustrates the coupling mechanism.

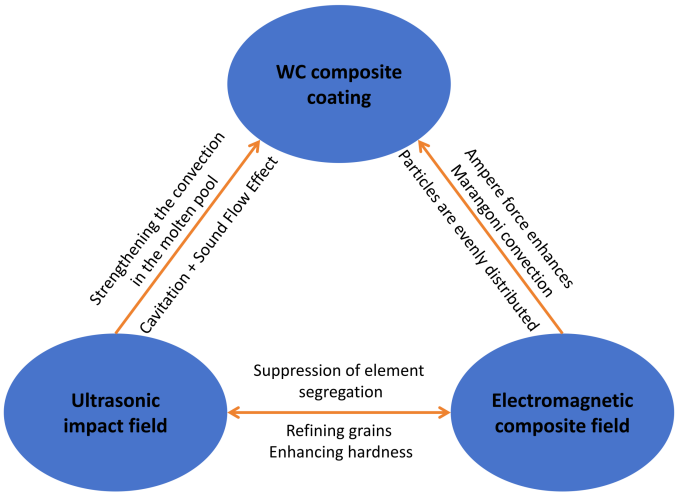


Fig. 1 Mechanism diagram of coupling effect

In the field of numerical modeling, researchers have established a multi-field coupled thermal-flow model in laser cladding processes conducting in-depth analyses of the thermal and flow field features within the molten pool, as well as the driving influence of Marangoni convection concerning the melt pool's flow dynamics. Bao et al. developed an inter-meso-scale dynamic model for the selective laser melting of nuclear-shell structure composite powders, studying the melting characteristics of WC/Ni composite powders and discovering that smaller particle size are more likely to form a molten pool. By appropriately controlling the laser power or scanning speed, the

aggregation of reinforcing particles can be prevented [13]. Luo et al. established a three-dimensional multiphase flow framework tailored specifically for NiCrBSi/WC composite powders in plasma transfer arc laser cladding, simulating the dispersion behavior of WC particles within the molten pool, and finding that under the influence of inward convection, WC particles are typically distributed near the centerline of the cladding layer [14]. To further clarify the mechanisms governing directional dispersion of WC particles, Wang et al. based on the thermal-flow-solid coupling model, deeply revealed that Marangoni convection is the dominant factor governing the fluid motion within the melt pool, and its flow velocity changes with the thermal gradient and the beam spot size. This study also pointed out that by optimizing process parameters, the even distribution of reinforcing particles in both the shallow and deep layers of the molten pool can be achieved, offering valuable theoretical direction for tailoring the coating's microstructure [15]. Regarding WC's effect on melt pool flow, it was found that the reaction of WC in the molten pool would release a substantial amount of heat energy, enabling the molten pool to achieve a faster flow rate. When the WC content was ≤ 10wt%, the flow rate increased rapidly, and when it was > 10wt%, the increase slowed down. WC caused the coating to precipitate more Cr-rich hard phases and intermetallic compounds.

Previous investigations have primarily concentrated on how macroscopic processing conditions influence the melt pool and resultant coating. However, the influence of WC particles' inherent properties (especially their particle size) has yet to be systematically studied on their movement behavior in the molten pool. In terms of numerical modeling, although some studies have used the thermal-fluid-solid coupling method to analyze the movement trajectories of WC particles within the molten pool, there are still few reports on systematic comparative studies of different particle size particles. The movement behavior of WC particles during laser cladding has two major characteristics: temporality and microscopism. This limits experimental observation. On the one hand, the time scale from the formation of the molten pool to its complete solidification is usually in the range of tens to hundreds of milliseconds. The movement, deceleration, and deposition process of WC particles in it is extremely short. Experimental methods are difficult to capture the final resting position of the particles at the moment of solidification. On the other hand, the WC particle size is at the micrometer scale, and the depth of the molten pool is approximately at the millimeter scale. Traditional non-contact sensors such as high-speed cameras and infrared temperature measurement are limited by spatial resolution and cannot accurately track the instantaneous movement trajectory and velocity change of individual particles within the molten pool. In contrast, the three-dimensional thermal-fluid-particle multi-

physics field coupling model established in this paper can break through the limitations of these time and space scales. By setting a very small time step and high-density output interval, it realizes the "frame-by-frame" replay of the entire movement process, thereby compensating for the lack of experimental ability to capture the transient state of solidification. At the same time, the model can output the micrometer-level precise coordinates of any particle at any time, without being limited by the spatial resolution of sensors; through statistical analysis of a large number of particles, it can quantitatively reveal the deposition depth, distribution range, and gradient characteristics of different particle size particles. In addition, the model allows independent control of parameters including laser power, scanning speed, powder feeding rate, particle size, and injection speed, eliminating accidental disturbances in experiments, and systematically studying the influence laws of a single factor (such as particle size) on the behavior of particles. Based on these advantages, this study takes laser cladding of Ni-based WC60 composite powder as the research object, using a combination of numerical modeling and experiments to systematically study the movement trajectories, velocity evolution, and final deposition distribution characteristics of five typical particle sizes (144 μm, 124 μm, 104 μm, 84 μm, 64 μm) of WC particles in the molten pool, aiming to reveal the regulatory mechanism of particle size on the movement behavior of WC particles and offer a theoretical foundation for optimizing the enhancement of phase space distribution through particle size selection.

Figure 2 presents the research framework of this paper. As shown in the figure, starting from the issue of uneven particle distribution in the laser cladding WC-Ni coating, the existing research progress and limitations are reviewed, and the three-dimensional thermal-flow-particle multi-physics field coupling model established in this paper is introduced. Through a systematic comparison of five typical WC particle size, the regulatory mechanism of particle size on the motion behavior and distribution is revealed, aiming to provide a theoretical basis for process optimization.

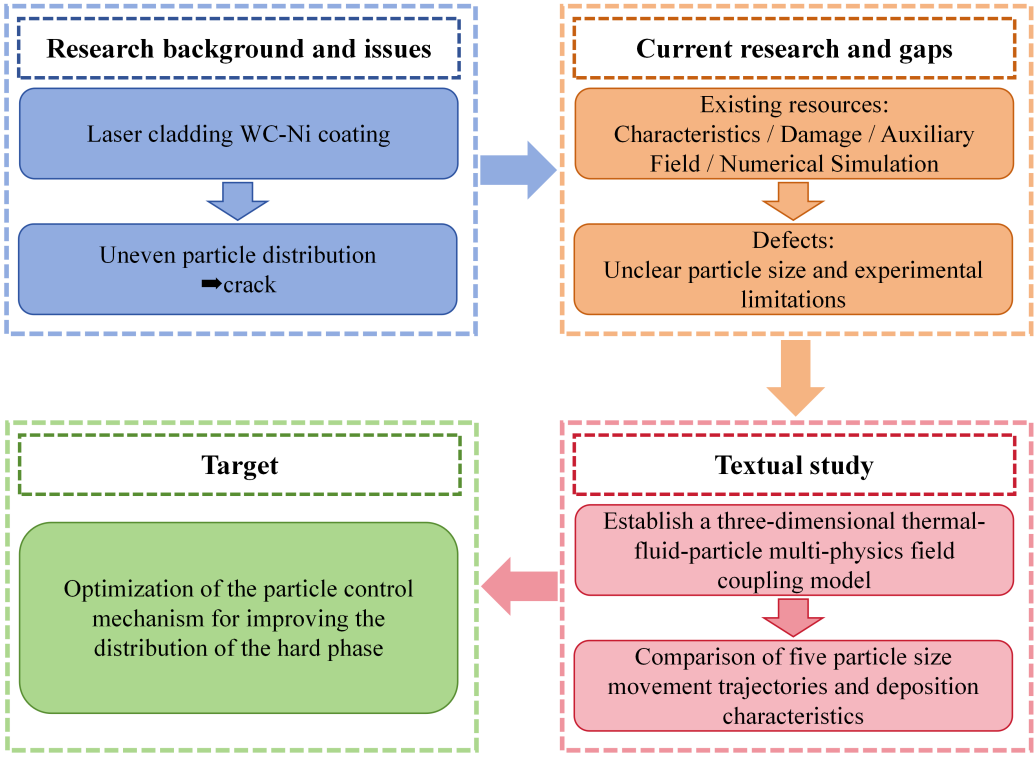


Fig.2 Schematic Diagram of Research Context

2 Selection and Experiment of Laser Cladding Materials

2.1 Laser cladding materials

42CrMo steel was selected as the substrate material in this study, with its chemical composition detailed in Table 1. This steel exhibits high strength, good toughness, and exceptional hardenability, making it a common choice for critical components such as gears and shafts.

Table 1 Elemental Composition of 42CrMo Steel, (wt.%)

Element	C	Si	Mn	Cu	Cr	Ni	Mo	Fe
Content	0.4	0.25	0.59	0.024	0.99	0.014	0.18	Bal.

The experiment selected nickel-based WC60 composite powder, with a composition of 60 wt% WC and 40 wt% nickel-based alloy. The powder morphology is spherical. To systematically study the effect of particle size on the movement behavior of WC particles, five representative particle sizes were selected: 144, 124, 104, 84, and 64 μm. The particle size distribution of the powder is shown in Fig. 3, and the main physical parameters are presented in Tables 2 and 3.

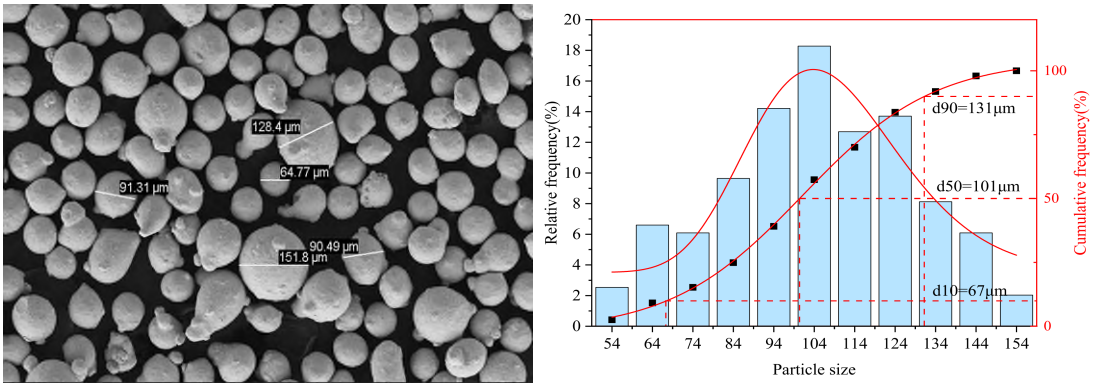


Fig. 3 Microscopic morphology characterization diagram of Ni-based WC60 powder

Table 2 Elemental Composition of Ni-based self-soluble Powders, (wt.%)

Element	C	Si	Mn	Cu	Cr	B	Fe	Ni
Content	0.6	4.3	0.2	5.2	16.5	3.2	10.6	Bal.

Table 3 Composition of WC powder elements, (wt.%)

Element	W	C
Content	96.05	3.95

2.2 Experimental process and sample preparation

Prior to laser cladding, both the substrate and powder require preliminary treatment. The 42CrMo substrate was initially polished with 200#-2000# sandpaper to obtain a smooth surface free of rust and scale. This was followed by cleaning with anhydrous ethanol and subsequent drying. The cladding process utilizes three coaxial powder feeders and employs a mechanical arm in conjunction with a TruDisk4002 disc laser from TRUMPF to perform single-pass laser cladding of WC60/Ni. The TruDisk4002 disc laser effectively converts rod-shaped crystals into disc crystals, thereby improving beam quality, enhancing power stability, and significantly elevating the overall performance of the laser cladding beam. The laser cladding system combining the disc laser and the mechanical arm is shown in Fig. 4. This laser can continuously output power ranging from 80W to 4000W, features a minimum fiber diameter of 200 μm, operates at a laser wavelength of 1030nm, and achieves a beam quality of up to 8mm·mrad.



Fig. 4 Laser cladding equipment diagram

3. Three-dimensional numerical simulation

This study established for the first time a three-dimensional transient thermal-fluid-particle multi-physical field coupling numerical model of the movement behavior of WC particles in the laser cladding of WC-reinforced Ni-based coatings, to clarify the movement characteristics of WC particles within the molten pool. The model is based on the following assumptions for simplification:

(1) The energy density of the laser heat source and the powder flow are Gaussian distributed；

(2) ssume that the liquid metal in the molten pool is an incompressible Newtonian fluid;

(3) Ignore the influence of powder on the molten pool; Simplify the irregular WC particles into ideal spheres and characterize them using average particle size or particle size distribution;

(4)WC particles, as the hard phase, are assumed to not melt or undergo phase transformation in the molten pool, but merely act as rigid particles to exchange momentum with the melt；

(5) Ignore the interaction forces between particles.

3.1 Governing Equations

Mass conservation is a fundamental law of fluid motion. For any fluid, the general form of the continuity equation is [16]：

$$\frac{\partial \rho_f}{\partial t} + \nabla \cdot (\rho_f u) = 0 \tag{1}$$

Herein, ρ_f represents the fluid density; u indicates the fluid velocity vector, and t denotes the time. This equation indicates that the rate of change in the mass with in the control body is equal to the net mass flow through its boundary.

According to the incompressible assumption, the density ρ_f is a constant. Therefore, $\partial\rho_f/\partial t = 0$ and $\nabla\cdot(\rho_f u) = \rho_f \nabla\cdot u$. Substituting equation (1) yields a simplified continuity equation:

$$\nabla\cdot u = 0 \tag{2}$$

This equation indicates that the velocity field divergence of incompressible fluids is zero, meaning that the volume flow rate flowing into any control body is equal to the outflow rate.

The laser cladding process is governed by the conservation equations for energy, momentum, and mass, which are respectively expressed as follows [17,18]:

$$\rho c_p \frac{\partial T}{\partial t} + \rho c_p \left(u\cdot\nabla\right)T = \nabla\cdot\left(k\nabla T\right) + Q_r + Q_x + Q_s - \nabla\cdot q \tag{3}$$

$$\rho\frac{\partial u}{\partial t} + \rho\left(u\cdot\nabla\right)u = \nabla\cdot\sigma + F \tag{4}$$

$$\frac{\partial\rho}{\partial t} + \nabla\cdot\left(\rho\boldsymbol{u}\right) = \dot{m}_{\text{source}} - \dot{m}_{\text{sink}} \tag{5}$$

Herein, ρ represents the material density; c indicates the specific heat capacity; T denotes the temperature; t stands for the time; k, the thermal conductivity; Q_r, the laser radiation heat transfer term; Q_x, the electromagnetic heat source term; Q_s, the other heat source term; q, the heat flux density; σ, the Cauchy stress tensor; F, the external force term; u, the velocity field; $\dot{m}_{\text{source}}$ and $\dot{m}_{\text{sink}}$ are the source term and the sink term, respectively. The expressions of the Cauchy stress tensor and the external force term are respectively as follows [19,20]:

$$\boldsymbol{\sigma} = -p\boldsymbol{I} + \mu\left(\nabla\boldsymbol{u} + \left(\nabla\boldsymbol{u}\right)^T\right) + \frac{2\mu}{3}\left(\nabla\cdot\boldsymbol{u}\right)\boldsymbol{I} \tag{6}$$

$$F = -K_0\frac{(1-f_1)^2}{f_1^3 + B}\mu \tag{7}$$

Herein, p represents fluid pressure; μ indicates the dynamic viscosity of the fluid; $\boldsymbol{u}$ denotes the fluid velocity vector; ∇ stands for the gradient operator; $\boldsymbol{I}$ represents the unit tensor (1 for diagonal elements and 0 for non-diagonal elements); K_0 indicates a

constant determined by the pore structure and its value is 2×10^7, and B denotes the minimum parameter to prevent division by zero, set to 10^{-3}. f represents the mass fraction of the liquid, and its expression is as follows：

$$f=\begin{cases}1 & T\geq T_l\\ \dfrac{T-T_l}{T_l-T_s} & T_s<T<T_l\\ 0 & T\leq T_s\end{cases} \tag{8}$$

Herein, T represents temperature, while T_s and T_l respectively denote the solid-phase line temperature and the liquid-phase line temperature.

When WC particles move in the molten pool, they are mainly subjected to the drag force, gravity and buoyancy exerted by the flow of the melt. Based on Newton's second law, the particle motion equation is given by [21]：

$$m_p\frac{d\boldsymbol{v}_p}{dt}=\boldsymbol{F}_d+\boldsymbol{F}_g+\boldsymbol{F}_b \tag{9}$$

$$m_p=\frac{4}{3}\pi r_p^3\rho_p \tag{10}$$

$$F_b=-\frac{4}{3}\pi r_p^3\rho_f g \tag{11}$$

Herein, m_p is the particle mass; r_p represents the particle radius; ρ_p indicates the WC particle density; v_p, the particle velocity vector; F_d, the drag force; F_g=$m_p g$, the gravity; F_b, the buoyancy; and ρ_f, the melt density.

3.2 Boundary and Parameter Definitions

Drag force is the main force exerted by the melt flow on the particles, and its magnitude depends on the relative velocity between the particles and the fluid, the particle size and the physical properties of the fluid. This study adopts the Schiller-Naumann drag model, whose expression is [22]：

$$F_d=\frac{1}{2}\rho_f C_D A_p\left|\boldsymbol{u}_f-\boldsymbol{v}_p\right|\left(\boldsymbol{u}_f-\boldsymbol{v}_p\right) \tag{12}$$

Herein, A_p=πr_p^2 is the projected area of the particle; u_f, the melt velocity vector; and C_D, the drag coefficient. The expression is as follows：

$$C_D=\frac{24}{Re_p}\left(1+0.15Re_p^{0.687}\right) \tag{13}$$

$$Re_p = \frac{\rho_f d_p |\boldsymbol{u}_f - \boldsymbol{v}_p|}{\mu_f} \tag{14}$$

Herein, Re_p is the Reynolds number of the particles and μ_f is the dynamic viscosity of the melt.

To quantitatively characterize the relative importance of inertial force and drag force, the Stokes number St is introduced. This quantity represents the particle relaxation time τ_p divided by the characteristic flow time τ_f of the molten pool [23]:

$$St = \frac{\tau_p}{\tau_f} \tag{15}$$

$$\tau_p = \frac{\rho_p d_p^2}{18\mu_f} \tag{16}$$

$$\tau_f = \frac{L}{U_f} \tag{17}$$

Herein, τ_p is the time scale of the particle velocity responding to the change in fluid velocity and τ_f is the time scale of molten pool flow. Take half the width of the molten pool L=1mm, the value of τ_f is calculated to be 4.55ms. Substituting the parameters of each particle size, the Stokes numbers of particles of each size were obtained: 0.56 for 144 μm, 0.42 for 124 μm, 0.29 for 104 μm, 0.19 for 84 μm, and 0.11 for 64 μm. When $St \ll 1$, the particles can quickly respond to the fluid motion and the drag force dominates their behavior; when $St > 0.4$, inertia takes over and the particles maintain their initial movement direction. The above calculation results provide a quantitative basis for the subsequent analysis of the influence of particle size on the particle movement patterns.

The control equations are supplemented with suitable conditions to specify the boundary constraints during laser cladding. The heat input follows a time-dependent Gaussian distribution, and its expression is as follows [24,25]:

$$q_{ener} = \frac{2\eta Q}{\pi r^2} \exp\left(\frac{-2(x - v_s t)^2 + y^2}{r^2}\right) - h_c(T - T_0) - \sigma_b \eth(T^4 - T_0^4) \tag{18}$$

Herein, Q represents the laser power; η indicates the laser absorption coefficient; v_s denotes the moving speed of the heat source; r stands for the radius of the laser beam; x and y represents the coordinates relative to the center of the heat source; h indicates the convective heat transfer coefficient; T_0 denotes the initial ambient temperature; σ stands for the Stefs-Boltzmann constant; and ε represents the material emissivity.

During the laser cladding process, the molten pool fluid motion is primarily governed by the Marangoni effect (originating from surface tension gradients) and buoyancy forces. The governing equations are presented below [26]:

$$F_c = -\rho g \beta (T - T_m) \tag{19}$$

$$\gamma = \gamma_1 - \gamma_0 (T - T_m) \tag{20}$$

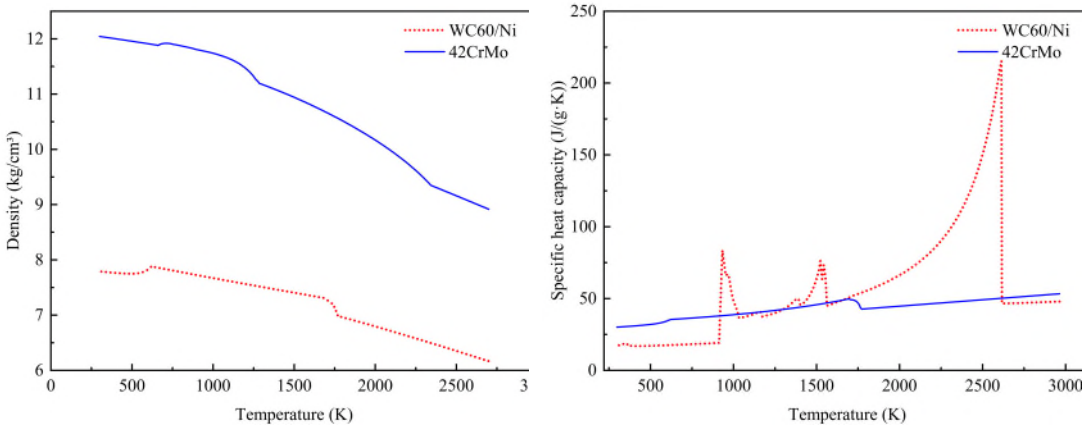
Herein, ρ represents the density of the molten metal; g indicates the acceleration due to gravity; β denotes the temperature gradient coefficient; T_m stands for the melting point of the metal; γ_1 represents the surface tension of the molten metal; and γ_0 indicates the temperature coefficient of the surface tension.

The forming process of the coating was simulated by the ALE method, and the expression of its motion equation is as follows [27]:

$$V_p = \frac{2 m_f \eta_m}{\rho_m \pi r_p^2} \exp\left(\frac{-2(x - V_d t)^2 + y^2}{r_p^2} \right) \dot{z} \tag{21}$$

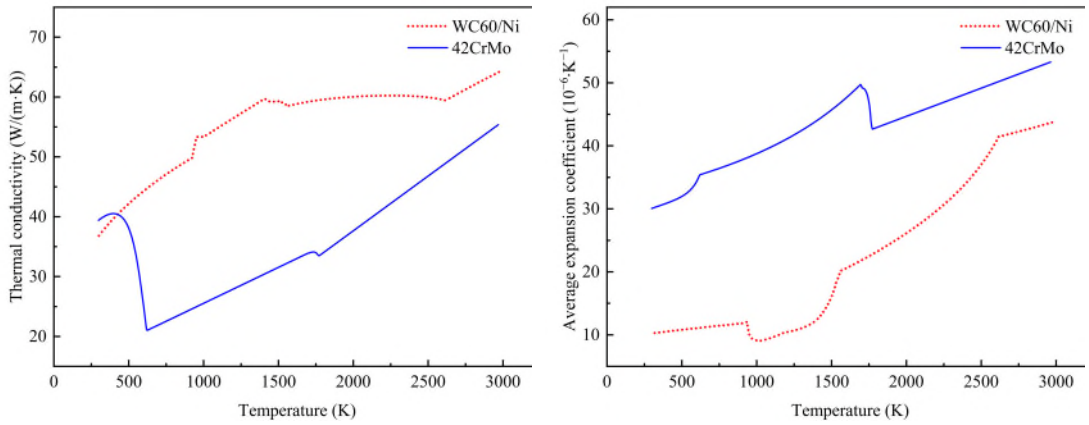
Herein, m_f represents the powder conveying rate; η_m indicates the powder collection efficiency; ρ_m denotes the powder density; r_p stands for the radius of the coating powder flow; and $\dot{z}$ represents the unit vector in the Z-axis direction.

The boundary condition process parameters of the model are as follows: the laser power Q is 1200W, the scanning speed v is 6.3mm·s, the spot radius r is 2mm, and the heat transfer coefficient h is 120W·m^{-2}·K^{-1}. The ambient temperature T_0 is 293.15K, the powder flow rate m_f is 6.2g/min, and the collection efficiency η_m is 0.8. The release interval of WC particles is 0.1ms to simulate the continuous powder feeding process. The particle sizes selected are 144, 124, 104, 84 and 64 μm, and they are released according to the particle size distribution ratio measured experimentally. The thermal physical parameter variation curves of WC60 nickel-based alloy powder and 42CrMo steel are shown in Fig. 5.



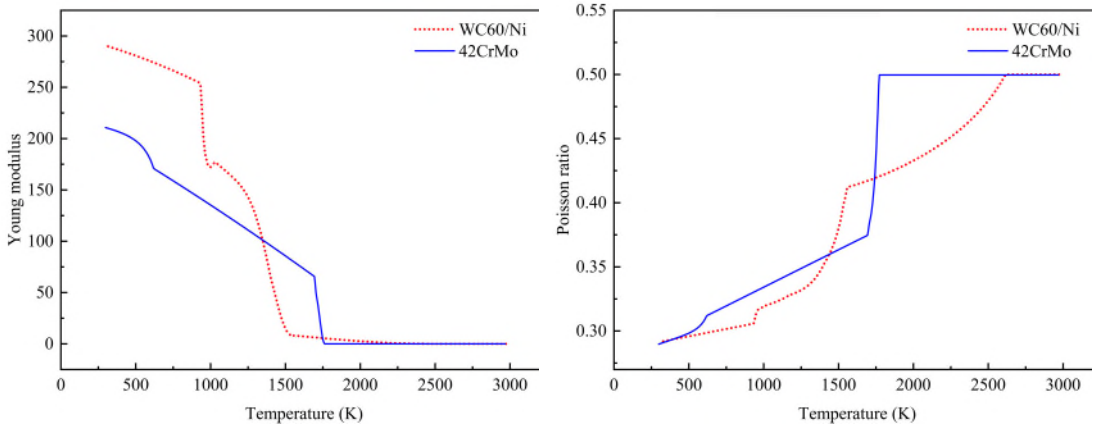
(a) Density

(b) Specific heat



(c) Heat conductivity coefficient

(d) Thermal expansivity



(e) Young modulus

(f) Poisson's ratio

Fig. 5 Thermal physical parameter variation curves of WC60/Ni powder and 42CrMo steel

3.3 Computational domain, mesh division and solution method

This model takes the rolls and cladding layers in the actual laser cladding experiment as the objects to establish a three-dimensional geometric model of the thermal-flow-particle multi-physical field. The rolls are simplified as hollow cylinders with a radius of 30mm, an axial length of 20mm, and an arc length covering an Angle of 45°(ranging from -6° to 39°). The cladding area is a circular ring structure with an outer radius of 30mm, an inner radius of 28.5mm, and a width of 6mm. Figure 6 displays the overall geometric model of the numerical model.

The model as a whole adopts free tetrahedral meshing. The cladding area is set with extremely fine meshing levels, and the hollow cylinder is set with ultra-fine meshing levels as shown in the figure. Among them, the maximum size of the extremely fine meshing element is 0.275mm, the minimum is 0.0179mm, the maximum growth rate is 1.08, the resolution of the narrow area is 0.95, and the curvature factor is 0.3. The model ultimately generates 206,472 domain units, 9,656 boundary elements and 400 edge units.

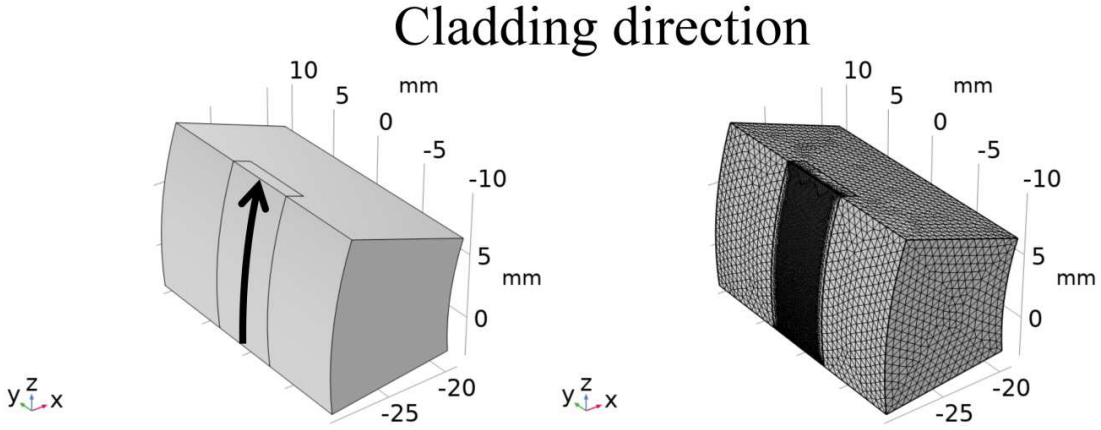


Fig. 6 Geometric Modeling and Meshing

The finite element method (FEM) is adopted in this work to solve the model. The time discretization adopts the implicit backward difference scheme (BDF), with the initial time step set to 1×10^{-5} s and the maximum time step limit set to 1×10^{-4} s to ensure sufficient time resolution during the stage of particle injection and rapid velocity changes. The temperature field and flow field are solved using a fully coupled transient solver, with the relative tolerance set to 1×10^{-4} and the absolute tolerance to 1×10^{-5}. For the nonlinear terms in the momentum equation, the Newton method is used for linearization, with a maximum number of iterations of 25 per time step. If convergence is not achieved, the time step is automatically reduced. The particle motion adopts a one-way coupling strategy: first, solve the temperature field and flow field until convergence, and save the flow field data at each time step; then, solve the particle motion equation in the converged flow field.

4. Results and Discussion

4.1 Characteristics of the temperature field and flow field of the molten pool

Knowledge of the molten pool's temperature and flow characteristics during laser cladding provides the foundation for interpreting WC particle motion. This section takes the moment when the particles stop releasing (t = 250ms) as a representative to analyze the temperature field and flow field characteristics within the molten pool. At this moment, the molten pool has entered a quasi-steady state, and no new particles will be injected thereafter, serving as the reference flow field for subsequent particle motion analysis. Based on numerical modeling for solution, this section analyzes the temperature field and flow field characteristics of the molten pool, providing a flow field basis for the subsequent particle motion analysis.

Figure 7(a) illustrates the temperature distribution cloud map of the molten pool at t = 250ms. The molten pool is typically semi-elliptical in shape, where the temperature is maximal at the center and then declines gradually to the edges. The computed peak temperature within the melt pool is about 2730 K, positioned close to the laser spot's center, far exceeding the liquidus temperature of the nickel-based alloy,

ensuring the full melting of the base material. The temperature field shows an asymmetric distribution along the laser scanning direction: the thermal gradient ahead of the moving heat source is steeper, whereas its trailing side exhibits a milder gradient, reflecting the heat accumulation phenomenon typical of a translating heat source.

Figure 8 demonstrates that Marangoni convection serves as the primary driver of liquid metal motion within the melt pool, which originates from surface tension variations. The surface temperature of the molten pool peaks at the center and decreases toward the periphery. The surface tension decreases as the temperature rises, propelling the liquid metal from the pool center toward the periphery, forming a main circulation radially outward. Figure 7(b) shows the velocity vector distribution at t = 250ms. Arrows point in the direction of flow, while their lengths are proportional to the velocity magnitude.

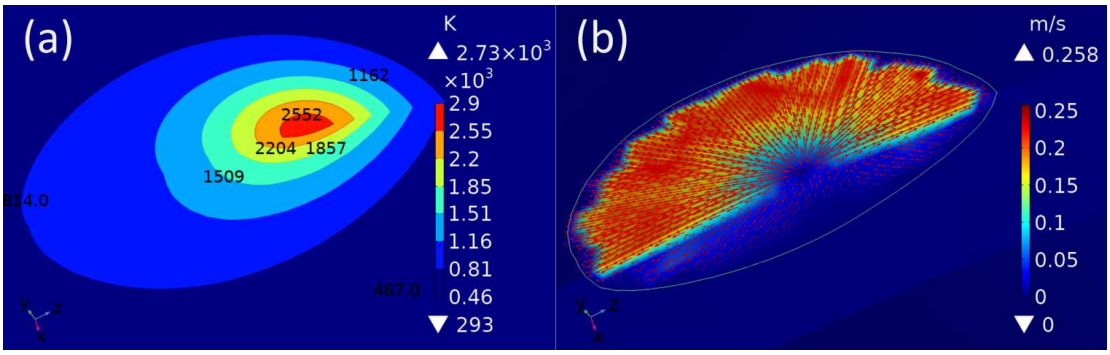


Fig. 7 Temperature and velocity cloud chart at 250ms

Based on the modeling and solution, the maximum flow velocity in the molten pool occurs in the outer ring area of the molten pool surface, and the maximum flow velocity is approximately 0.258 m/s. This region resides at the free surface of the melt pool, where the surface tension gradient serves as the driving force, and the flow velocity attains its maximum. The central region exhibits a comparatively low flow velocity as a result of the reduced temperature gradient. The flow velocity in the edge area also gradually decreases. This velocity distribution of "low center, high outer ring, and low edge" is a typical feature of Marangoni convection: the surface tension gradient drives the melt to accelerate outward from the center, reaching a peak in the outer ring, and then decelerates due to viscous dissipation.

The above-mentioned flow field characteristics have a direct influence on the movement of WC particles. The particles located in the outer ring area of the molten pool surface are subjected to a stronger drag force and are expected to have a higher horizontal velocity and a larger horizontal offset. This prediction is verified in the particle trajectory analysis in Section 4.2. In the peripheral region of the melt pool, the flow speed is comparatively low, making particles susceptible to retention or accumulation, which is consistent with the observation that fine particles are ultimately

distributed at the edge of the molten pool. After 250 ms, the injection of new particles was stopped. The motion of the introduced particles was entirely governed by the flow field, providing clear initial conditions for analyzing the movement and deposition behavior of the particles.

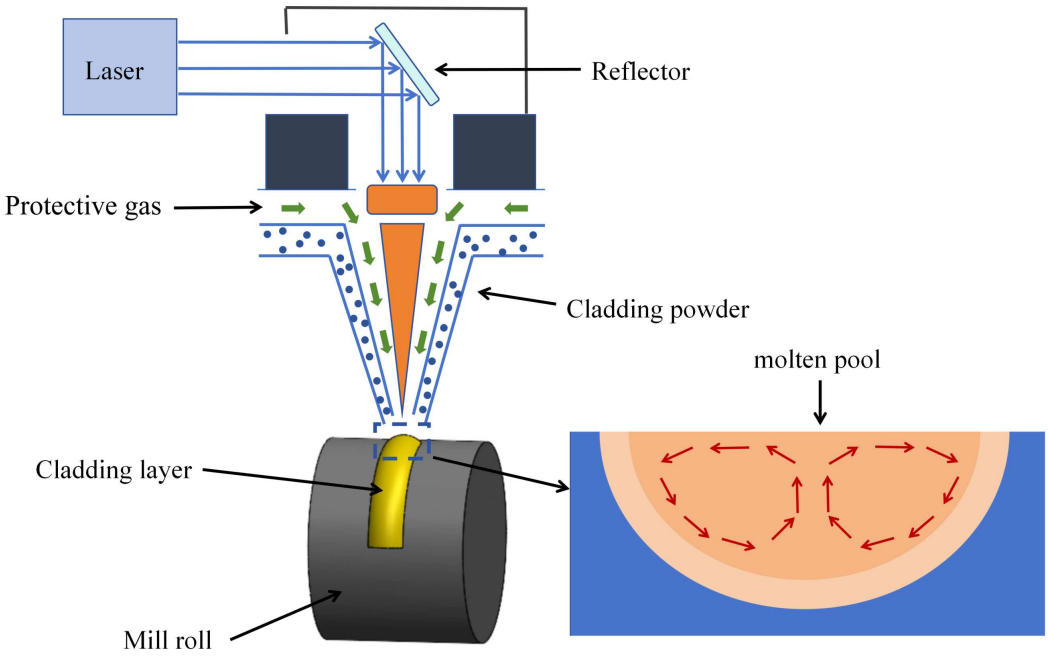


Fig. 8 Schematic of Marangoni convection

4.2 The influence of particle size on the movement trajectory of WC particles

The movement trajectory of WC particles in the molten pool reflects their force state and movement pattern, and it is the most intuitive basis for understanding the particle size effect. Figures 9-13 show the typical movement trajectories of particles of various sizes in the molten pool (colors indicate particle velocities, blue for low speed and red for high speed; arrows indicate the direction of particle velocities).

Figure 9 shows that the 144 μm particles move along approximately straight lines, showing a slight horizontal displacement. The overall trend is to sink diagonally. The particles entering the center of the molten pool sink vertically, and all the particles sink to the bottom at 272ms. The particles directly sink from the injection point to the bottom of the molten pool, and throughout the process, there is no horizontal transport or retention along the surface of the molten pool. The inclination Angle of the trajectory is very small, indicating that its movement direction is minimally affected by the Marangoni convection. This characteristic is attributed to the large inertia of the 144 μm particles. Their Stokes number $St = 0.56 > 0.4$, relaxation time $\tau_p = 2.56\text{ms}$ are of the same order of magnitude as the characteristic time of the molten pool flow $\tau_f \approx 4.55\text{ms}$. The particles can resist the drag force and basically maintain their initial motion direction, being only subject to extremely weak flow disturbances.

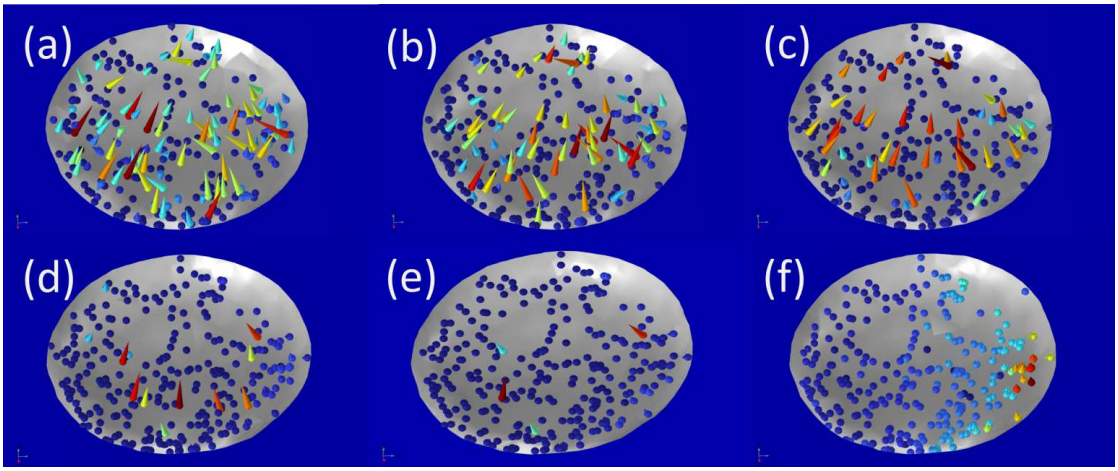


Fig. 9 Temporal evolution of 144 μm WC particle movement within the molten pool at: (a) 251 ms, (b) 255 ms, (c) 259 ms, (d) 264 ms, (e) 267 ms, (f) 272 ms.

As shown in Fig. 10, the trajectory of the 124 μm particles is also approximately a straight line. All of them reached the bottom at 277 ms. Compared with the 144 μm particles, the inclined angle of their downward sinking is slightly larger, and the horizontal displacement is more obvious. This behavior indicates that although the inertia of the 124 μm particles has dominated the motion (St = 0.42 > 0.4), its lower Stokes number compared to the 144 μm particles makes it slightly more sensitive to Marangoni convection, showing a slightly larger horizontal deflection. The 124 μm particles still did not exhibit any horizontal transport or floating along the surface, and all stabilized and sank to the bottom.

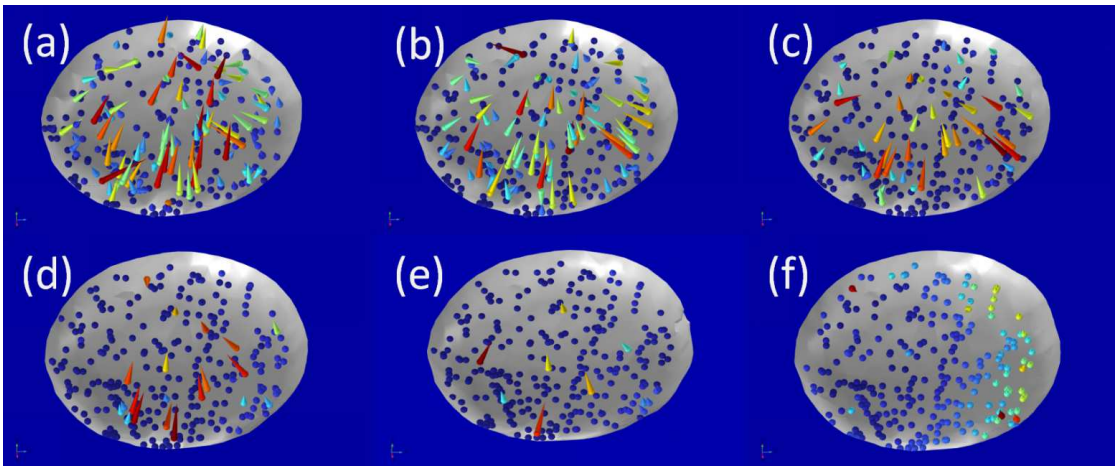


Fig. 10 Temporal evolution of 124 μm WC particle movement within the molten pool at: (a) 251 ms, (b) 255 ms, (c) 259 ms, (d) 268 ms, (e) 273 ms, (f) 277 ms

As shown in Fig. 11, the movement behavior of 104 μm particles is not a single pattern but presents two different trajectory characteristics. Some particles descend directly towards the bottom of the molten pool in a slanting downward manner, with a more significant inclination angle than that of 124 μm particles, indicating that inertia has taken effect but is still significantly modulated by the molten pool's flow dynamics.

The other particles exhibit a clear horizontal displacement, moving along the surface or shallow layer of the molten pool to below the edge of the pool. These two patterns coexist in the 104 μm particles, forming a mixed distribution feature of "partially slanting downward and partially moving horizontally to below the edge". This particle size St = 0.29 is in the intense competition zone between drag force and inertial force, and the final movement pattern of the particles depends on the injection position and local flow field conditions.

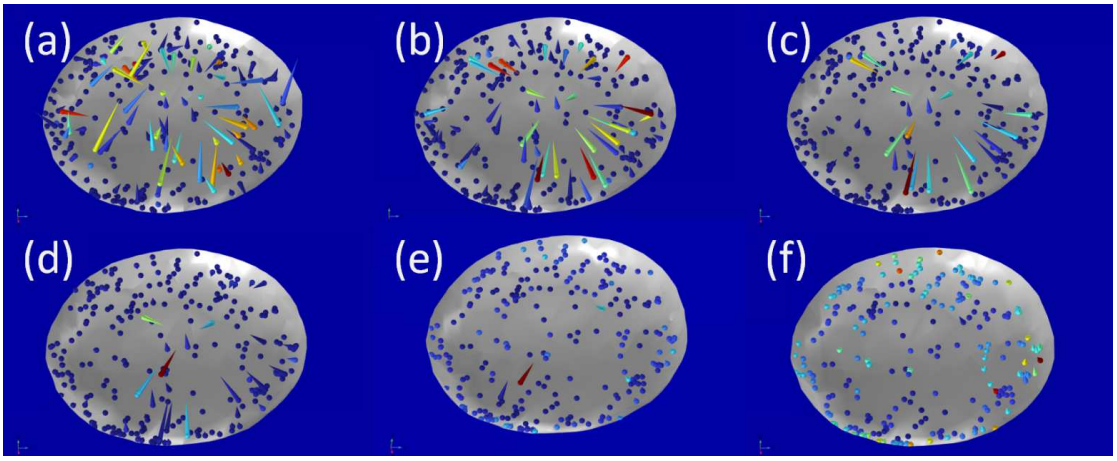


Fig. 11 Temporal evolution of 104 μm WC particle movement within the molten pool at: (a) 251 ms, (b) 255 ms, (c) 259 ms, (d) 268 ms, (e) 275 ms, (f) 281 ms

As shown in Figures 12 and 13, neither the 84 μm nor the 64 μm particles exhibited an active sinking trend. Instead, they moved in a slanting downward direction towards the edge of the molten pool. The movement trajectory was mainly horizontal, accompanied by a limited sinking component. Upon entry into the melt pool from the release point, the 84 μm particles were quickly captured by Marangoni convection and moved in a slanting downward direction towards the edge of the molten pool. The trajectory was in a gentle slope shape, with significant horizontal displacement and limited vertical displacement. The movement direction was mainly horizontal, and there was no vertical sinking like that of the coarse particles. The movement behavior of the 64 μm particles was similar to that of the 84 μm particles, but the sinking distance was smaller, and the vertical displacement was very small. These differences indicate that as the particle size decreases (from 84 μm to 64 μm), the inertia of the particles slightly decreases, allowing them to obtain a smaller sinking component during the horizontal movement, and overall they still belong to a slanting horizontal movement dominated by drag force, which is fundamentally different from the inertia-dominated sinking of the coarse particles. As the molten pool moved, the front side of the molten pool began to melt, and the particles on the front side would follow the Marangoni convection and be transported to the lower part of the molten pool.

In order to reveal the dynamic behavior of fine particles after they stop releasing, taking particles with a size of 84 μm as an example, the particles marked with red circles in Fig. 12 represent the movement of a single particle that reached the bottom of the molten pool 250 ms later. At 251 ms, this particle was located below the edge of the molten pool and was then drawn into the Marangoni convection. In this flow field, the particles located below the edge are subjected to the combined action of multiple directional resistance forces, and their movement direction changes constantly, eventually migrating along the circular path at the center of the molten pool and approaching the center of the pool at 275 ms. At 281 ms, it moved upward with the Marangoni convection; at 283 ms, the particle was close to the surface of the molten pool, and at this time, the flow direction changed to the horizontal direction, and the direction of the particle's speed was approximately horizontal; at 293 ms, it reached the edge. The behavior of 64 μm particles is similar to that of 84 μm particles, but the response time is slightly different. The above observation results indicate that particles of 84 μm and 64 μm can quickly respond to the continuous Marangoni convection, be carried upward, and move horizontally by the Marangoni convection, gather at the edge of the molten pool, which is a typical manifestation of following the flow characteristics under a low Stokes number $St < 0.2$.

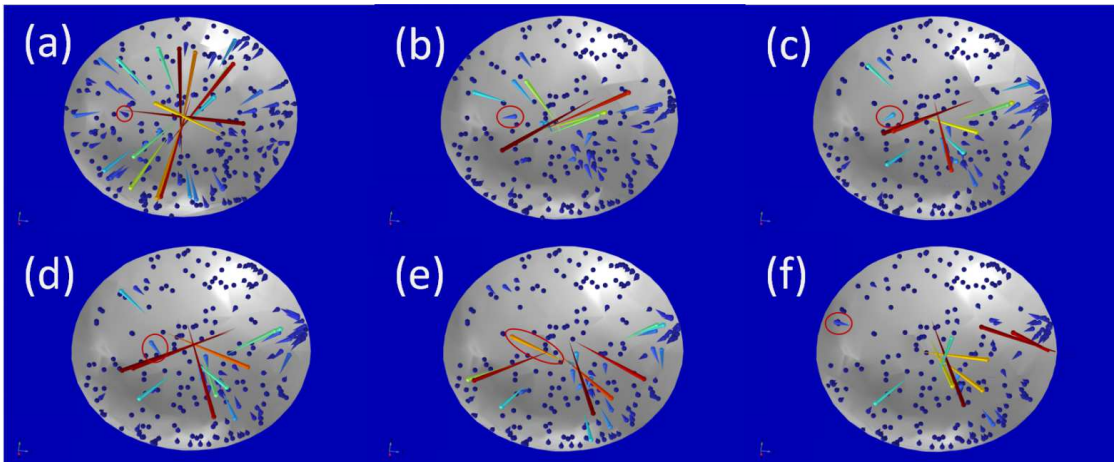


Fig. 12 Temporal evolution of 84 μm WC particle movement within the molten pool at: (a) 251 ms, (b) 275 ms, (c) 281 ms, (d) 283 ms, (e) 286 ms, (f) 293 ms

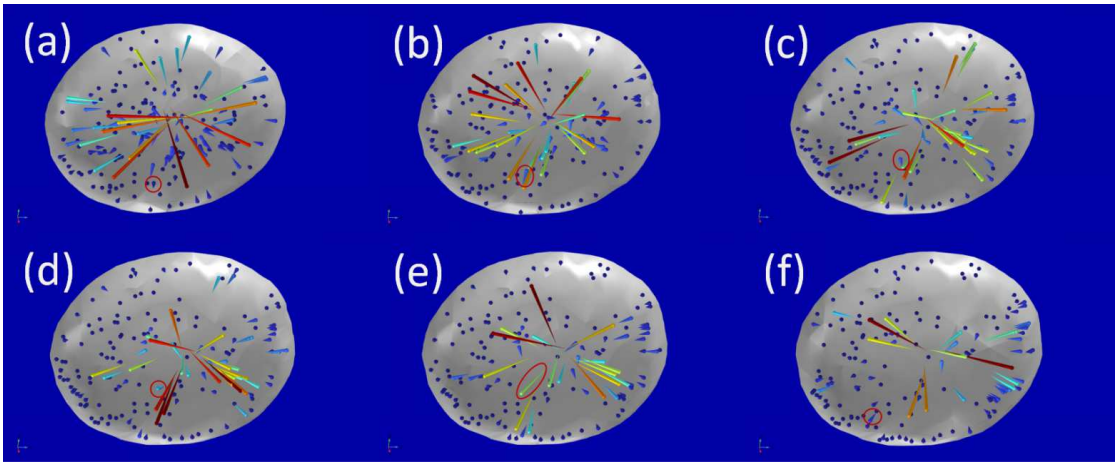


Fig. 13 Temporal evolution of 64 μm WC particle movement within the molten pool at: (a) 251 ms, (b) 268 ms, (c) 277 ms, (d) 280 ms, (e) 285 ms, (f) 294 ms

The above analysis indicates that particle size is one of the important factors determining the movement pattern of particles. However, within the same particle size group, the movement trajectories of the particles still vary, which is closely related to the injection position. According to the flow field analysis in Section 4.1, the surface flow velocity of the molten pool is not uniformly distributed: the velocity is lower at the center of the molten pool, gradually increases outward, reaches the maximum value in the outer ring area of the surface, and then decreases towards the edge. Therefore, particles injected into the region with the maximum flow velocity will be subjected to stronger drag force. Taking 104 μm particles as an example, particles injected into the region with the maximum flow velocity have a higher initial horizontal velocity and a significantly greater horizontal displacement than those injected at the center or edge; at the same time, the particles are accelerated in the horizontal direction, much higher than those injected into other areas. This phenomenon also exists in fine particles (84 and 64 μm): fine particles injected into the region with the maximum flow velocity have a faster horizontal movement speed and reach the edge of the molten pool in a shorter time. For coarse particles (144 and 124 μm), due to the dominance of inertia, the injection position has a relatively small influence on their movement direction, but the drag force in the region with the maximum flow velocity can still cause a slight increase in their horizontal displacement. The results show that the final movement trajectory of the particles not only depends on the particle size, but also is affected by their injection position.

4.3 Effect of WC particle size on Distribution Characteristics

The deposition and distribution characteristics of WC particles in the coating layer, including the distribution range, spatial position and uniformity, directly determine the macroscopic arrangement of the reinforcing phase and are an important basis for

evaluating the uniformity and gradient structure of the coating performance. In this study, 300ms was selected as the observation time for the deposition distribution characteristics. For coarse particles (144 and 124 μm) and medium particles (104 μm), the particles had basically completed deposition and their movement had stabilized at this time; for fine particles (84 and 64 μm), they were still in the dynamic motion process dominated by Marangoni convection at this time, and the distribution characteristics could already reflect the final trend. Fig. 14 shows six distribution diagrams: Fig. 14(a) is the superimposed distribution of all particle sizes (different colors represent different particle sizes); Figures 14(b)-(f) are the individual distributions of 144, 124, 104, 84, and 64 μm particles (colors represent the deposition depth, blue for shallow layer, red for deep layer).

Figures 12(b) and (c) illustrate that the deposition distribution of 144 μm and 124 μm particles is highly concentrated and has good uniformity. All particles are deposited in the bottom area of the molten pool, and they are arranged closely and uniformly among each other. The distribution area of 144 μm particles is slightly smaller than that of 124 μm particles. Neither of them shows obvious edge aggregation or local accumulation. This distribution feature indicates that the coarse particles are dominated by inertia ($St > 0.4$), and all of them sink to the bottom at t = 300ms. The particle quantity is moderate and the movement trajectory is stable, forming an evenly enriched area of the reinforcing phase at the bottom.

Figure 14(d) indicates that the deposition distribution of 104 μm particles exhibits a distinct outer ring feature: the distribution density of the particles in the central area of the bottom of the molten pool is significantly lower than that of the coarse particles, and they are concentrated in the outer ring area around the bottom center and below the edge of the molten pool. The distribution area is larger than that of 124 μm particles, and there is no dense stacking at the bottom center. This distribution feature indicates that the 104 μm particles are in the competition zone between drag force and inertial force ($St = 0.29$). At t = 300 ms, all the particles have settled at the bottom, and affected by the horizontal movement of Marangoni convection, the particles are mainly carried to the outer ring and the lower edge for deposition, forming a distribution feature with sparse centers and enriched outer ring and edges.

Figures 14(e) and (f) demonstrate that the deposition distribution of 84 μm and 64 μm particles exhibits distinct dispersion and edge aggregation characteristics. The 84 μm particles are mainly distributed at the edge of the molten pool and in the upper, middle, lower (lower part) and upper-middle-lower (upper part) regions. The distribution range is wide, with higher density at the edge and fewer in the central area. The 64 μm particles are also mainly located at the edge and the upper-middle-lower

(upper part) regions of the molten pool, but they are more inclined towards the upper part compared to the 84 μm particles, with a wider distribution range and more significant edge aggregation phenomenon. Neither of the two types of particles form a distinct accumulation layer at the bottom of the molten pool. There is no close arrangement between the particles, and the overall state is a loose dispersion. This distribution feature indicates that the fine particles are dominated by drag force (St < 0.2), and at t = 300 ms, they have basically been horizontally transported to the edge of the molten pool by Marangoni convection. The particle quantity is moderate but the movement trajectories are significantly modulated by the flow, and finally, a dispersed and edge-enriched enhanced phase distribution area was formed in the edge and upper-middle-lower regions. Reducing the particle size from 84 μm to 64 μm leads to a modest reduction in sinking distance.

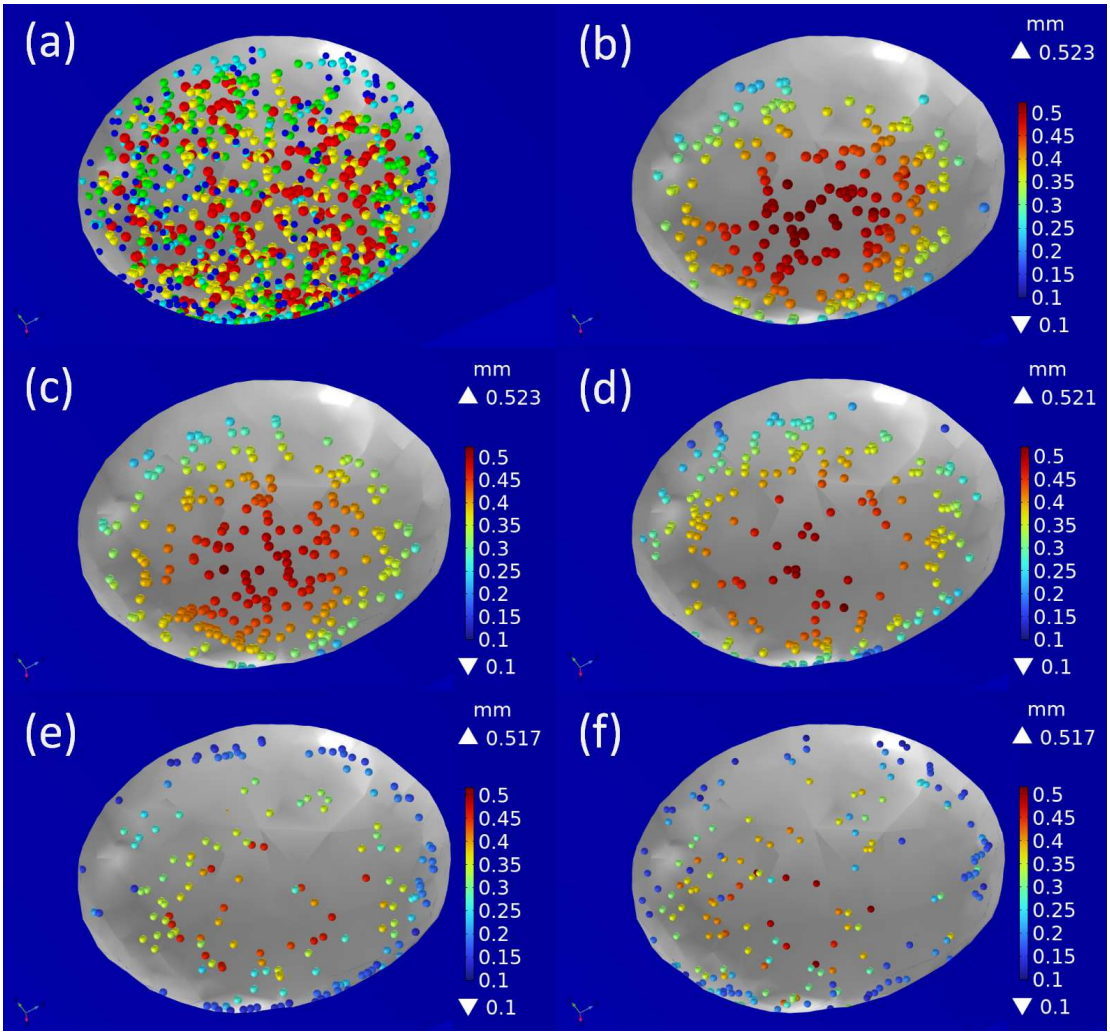


Fig. 14 Spatial distribution of deposited WC particles of varying diameters at 300 ms: (a) overlay of five sizes (red: 144 μm, yellow: 124 μm, green: 104 μm, cyan: 84 μm, blue: 64 μm), (b) 144 μm, (c) 124 μm, (d) 104 μm, (e) 84 μm, (f) 64 μm

The deposition distribution characteristics of particles of various sizes are

summarized in Table 4. As the particle size decreases, the deposition distribution gradually transitions from "concentration at the bottom" to "diffusion at the edges". This pattern can be uniformly explained by the Stokes number: when $St > 0.4$ (144 and 124 μm), inertia dominates, and the particles sink directly to the bottom and are uniformly distributed throughout the bottom; when $St = 0.29$ (104 μm), drag force competes with inertia, and the particles are partially thrown to the outer ring during horizontal movement, but still a certain number reach the center, forming a distribution with a central density in the middle and enrichment in the outer ring; when $St < 0.2$ (84 and 64 μm), drag force dominates, and the particles are difficult to reach the bottom, mainly distributed at the edges and the middle and lower parts. This discovery provides a quantitative basis for regulating the spatial distribution uniformity and gradient structure of the reinforcing phase through particle size selection.

Table 4 Spatial distribution characteristics of WC particles with different diameters

particle size (μm)	Spatial distribution	Central area concentration	Relative spread of distribution
144	Bottom	Highest	Smallest
124	Bottom	Hight	Smaller
104	Outer ring of bottom and below edge	Moderate	Medium
84	Edge and middle-lower region (lower part)	Low	Larger
64	Edge and middle-upper region (upper part)	Lower	Largest

4.4 Model Validation and Analysis

As illustrated in Fig. 15, to validate the numerical approach, the coating morphology was experimentally measured and relative to the model results. Through the horizontal comparison of GT (numerical calculation of the coating cross-sectional profile) and RS (scanning electron microscope observation of contour heights), the WC particles were readily visible in the cross-sectional view of the sample, with their typical

feature being light-colored small spheres. Table 5 lists the experimental and model data comparisons of the contour heights and widths of the coating, with an error of 3.33% and 3.04%, which is within the allowable range. This key result directly verifies the accuracy of the numerical model method, laying a reliable foundation for the subsequent analysis of particle distribution in the flow field and temperature field.

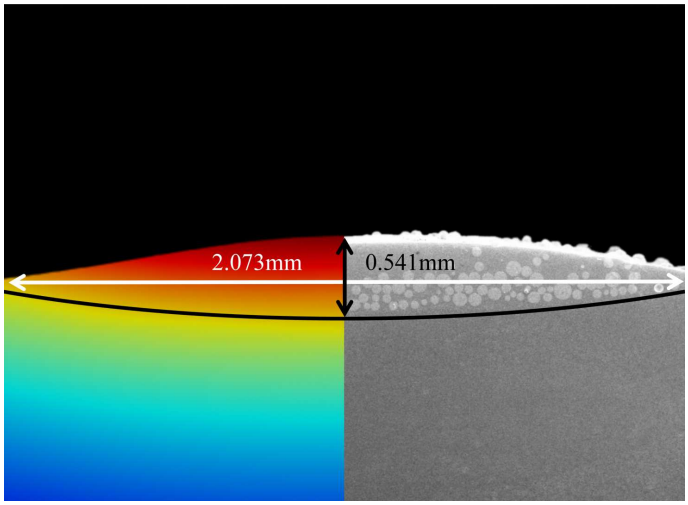


Fig. 15 Comparison Chart of Coating Morphology

Table 5 Comparison of Coating Profile Heights

Experimental height (mm)	Simulated height (mm)	Relative error (%)	Experimental width (mm)	Simulated width (mm)	Relative error (%)
0.541	0.523	3.33	2.073	2.01	3.04

As illustrated in Fig. 16, in terms of the lateral distribution characteristics of the particles, the WC particles exhibit a distinct enrichment feature on both sides in the transverse section of the cladding layer: the distribution density of the particles in the left and right edge areas of the molten pool is significantly higher than that in the central area. This phenomenon is particularly evident in fine particles, and coarse particles also have a certain tendency to aggregate at the edges. The model solution results are highly consistent with the experimental observations: the 84 μm and 64 μm particles are mainly distributed at the edge and upper-middle-lower parts of the molten pool, with scarce particles in the central area; the 104 μm particles are enriched in the outer ring at the bottom and below the edge, with a lower degree of aggregation in the central area; the 144 μm and 124 μm particles are mainly concentrated at the bottom, but their distribution range also shows a trend of center-to-edge aggregation. Both of them qualitatively match the "particle aggregation towards the molten pool edge" lateral distribution characteristic, confirming the model's reliability in capturing the horizontal transport behavior of particles driven by Marangoni convection.

In terms of the vertical distribution of particles, the model solution results are consistent with the observations from the electron microscope experiments, but there are also explainable differences. The experiments revealed that not all the coarse particles were deposited at the bottom of the molten pool: some of the coarse particles were directly deposited at the bottom, while others were blocked by the previously deposited fine particle layers and remained in the middle of the molten pool. Medium-sized particles predominantly resided in the middle and lower transitional areas. Fine particles were detected across the entire depth of the molten pool (upper, middle, and lower regions) and also at the periphery, showing a wide vertical distribution range. The model solution results indicated that all the coarse particles were deposited at the bottom of the molten pool, without any retention in the middle; medium-sized particles were located in the middle and lower parts; and fine particles could be seen in the upper, middle, and lower parts of the molten pool as well as on the edges, with a wide distribution range.

The main difference between the model and the experiment in the vertical distribution of coarse particles lies in the following: in the model, all coarse particles reach the bottom, while in the experiment, some coarse particles are blocked by the fine particle layer and fail to sink to the bottom. This difference stems from the assumption of the model: particles are regarded as volumeless geometric points, ignoring the volume exclusion and collision effects between particles. In the real physical process, the fine particles that deposit first will occupy the bottom of the molten pool, thereby creating a physical obstruction. Some coarse particles, due to their larger size, cannot pass through the gaps of the fine particle pile and are blocked in the middle; while in the model, the coarse particles can "penetrate" the fine particle layer without hindrance and all reach the bottom. Despite this, the model and the experiment are consistent in the core trends of extensive distribution of fine particles, transitional distribution of medium particles, and overall downward bias of coarse particles. This verifies the validity of the model. There are limitations in the model's solution process regarding the fine stacking sequence between particles and the phenomenon of coarse particles being blocked and remaining in the middle. However, as a whole, it is applicable to guiding the regulation of the spatial distribution of the reinforcing phase through particle size selection. Subsequent studies could integrate the Discrete Element Method (DEM) with Computational Fluid Dynamics (CFD) to incorporate the effects of particle volume exclusion and collisions, further improving the prediction accuracy of particle stacking behavior.

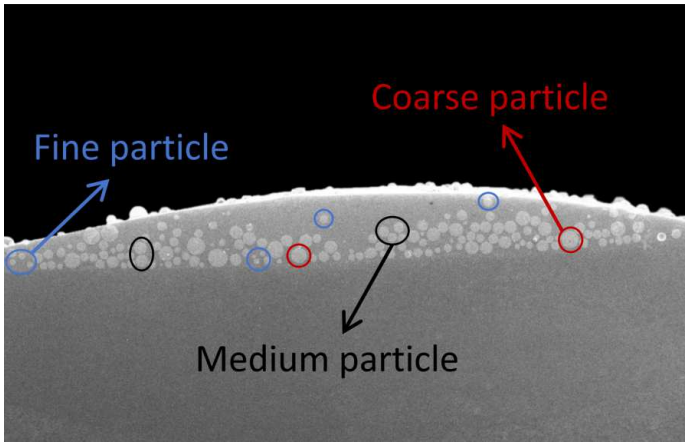


Fig. 16 Scanning electron microscope image of the cross-sectional profile of the nickel-based WC60 composite cladding layer

5. Conclusion

This paper focuses on the movement behavior of WC particles during laser cladding of nickel-based WC60. A transient 3D thermal-flow-particle multi-physics field coupling model was established, and the model was experimentally validated. Based on this model, the movement trajectories and deposition distribution laws of five representative particle size (144, 124, 104, 84 and 64 μm) of WC particles in the molten pool were systematically studied. The main conclusions are as follows:

(1) A multi-physics field coupling numerical model for the motion behavior of WC particles in laser cladding was established. This model integrates the moving heat source, Marangoni convection and particle drag force, effectively predicting the motion trajectories and deposition distribution of WC particles of different diameters, and making up for the deficiency of existing models in the systematic study of the particle size effect.

(2) The particle size significantly regulates the movement trajectory of WC particles. Coarse particles (144 and 124 μm) are dominated by inertia and sink obliquely downward; fine particles (84 and 64 μm) are dominated by drag force and move horizontally towards the edge through Marangoni convection; medium-sized particles (104 μm) exhibit transitional behavior. The particle size effect can be quantitatively described by the Stokes number.

(3) Particle size controls the deposition distribution of WC particles. The coarse particles are all concentrated at the bottom, with a highly concentrated distribution; the fine particles are dispersed at the edges and in the upper, middle and lower parts, with a significant enrichment at the edges; the medium-sized particles are located in the middle and lower parts. As the particle size decreases, the distribution transitions from

"concentration at the bottom" to "diffusion towards the edges" in a gradient manner.

Acknowledgments

This work was supported by the Fundamental Research Funds for the Liaoning Universities(LJ222410146021), Fundamental Research Funds for the Liaoning Universities(LJ232510146003).

Author contributions

Sen Wang and Chang Li are responsible for the writing of the paper and the numerical modeling work, and experimental work. Chuang Wang, Chuanbin Ma, Wenping Xu and Xing Han contributed to data extraction and format correction of the article. All the authors read and approved the final manuscript.

Data Availability

The data that support the findings of this study are available from the corresponding author upon reasonable request.

Competing interest

The authors declare that they have no known competing financial interests or personal relationships that could have appeared to influence the work reported in this study.

References

[1] S. Sun, J. Wang, J. Xu, X. Cheng, C. Jing, Z. Chen, H. Ru, Y. Liu, and J. Jiao, Preparing WC-Ni coatings with laser cladding technology: A review. Mater. Today Commun. **37**, 106939 (2023). https://doi.org/10.1016/j.mtcomm.2023.106939

[2] A. Ortíz, A. García, M. Cadenas, M.R. Fernández, and J.M. Cuetos, WC particles distribution model in the cross-section of laser cladded NiCrBSi + WC coatings, for different wt% WC. Surf. Coat. Technol. **324**, 298–306 (2017). https://doi.org/10.1016/j.surfcoat.2017.05.086

[3] Z.K. Weng, A.H. Wang, X.H. Wu, Y.Y. Wang, and J.X. Yang, Wear resistance of diode laser-clad Ni/WC composite coatings at different temperatures. Surf. Coat. Technol. **304**, 283–292 (2016). https://doi.org/10.1016/j.surfcoat.2016.06.081

[4] W. Li, R. Di, R. Yuan, H. Song, and J. Lei, Microstructure, wear resistance and electrochemical properties of spherical/non-spherical WC reinforced Inconel 625 superalloy by laser melting deposition. J. Manuf. Process. **74**, 413–422 (2022). https://doi.org/10.1016/j.jmapro.2021.12.045

[5] J.S. Xu, X.C. Zhang, F.Z. Xuan, Z.D. Wang, and S.T. Tu, Microstructure and sliding wear resistance of laser cladded WC/Ni composite coatings with different contents of WC particle. J. Mater. Eng. Perform. **21**, 1904–1911 (2012). https://doi.org/10.1007/s11665-011-0109-8

[6] Z. Hu, Y. Li, B. Lu, N. Tan, L. Cai, and Q. Yong, Effect of WC content on microstructure and properties of high-speed laser cladding Ni-based coating. Opt. Laser Technol. **155**, 108449 (2022). https://doi.org/10.1016/j.optlastec.2022.108449

[7] N. Tan, Z. Hu, Y. Zhou, Y. Li, B. Lu, D. Hu, Y. Liu, and Q. Li, Effect of WC particle size on the microstructure and tribological properties of high-speed laser cladding Ni/WC composite coatings. Mater. Today Commun. **39**, 109066 (2024). https://doi.org/10.1016/j.mtcomm.2024.109066

[8] C. Zhang, W. Sun, E. Liu, Y. Liu, J. Liu, B. Zhang, M. Zhou, Y. Xu, and Y. Jia, Effects of particle size and content of cladding powder on in situ synthesized WC-reinforced Ni-based cladding layers. Int. J. Appl. Ceram. Technol. **21**, 1625–1637 (2024). https://doi.org/10.1111/ijac.14609

[9] X. Wang, S. Zhou, X. Dai, J. Lei, J. Guo, Z. Gu, and T. Wang, Evaluation and mechanisms on heat damage of WC particles in Ni60/WC composite coatings by laser induction hybrid cladding. Int. J. Refract. Met. Hard Mater. **64**, 234–241 (2017). https://doi.org/10.1016/j.ijrmhm.2016.11.001

[10] L. Wang, J. Luo, Y. Hu, H. Xia, and J. Yao, Study on process parameters of coaxial laser melt inj ection with spherical WC reinforcement particles. J. Mech. Eng. **57**, 253–261 (2021). https://doi.org/1 0.3901/JME.2021.07.253

[11] J. Chen, Z. Yao, F. Wang, Y. Chi, Z. Wang, S. Tofil, and J. Yao, Grain refinement and Laves phas e dispersion by high-intensity ultrasonic vibration in laser cladding of Inconel 718. J. Mater. Res. T echnol. **30**, 8563–8575 (2024). https://doi.org/10.1016/j.jmrt.2024.05.229

[12] K. Huo, J. Zhou, F. Dai, and J. Xu, Particle distribution and microstructure of IN718/WC composite coating fabricated by electromagnetic compound field-assisted laser cladding. Appl. Surf. Sci. **545**, 149078 (2021). https://doi.org/10.1016/j.apsusc.2021.149078

[13] T. Bao, Y. Tan, and Y. Xu, Mesoscopic simulation of core–shell composite powder materials by sele ctive laser melting. Materials **16**, 7005 (2023). **https://doi.org/10.3390/ma16217005**

[14] L. Luo, X. Bai, C. Luo, Z. Wang, X. Liang, and L. Wen, Modeling of multi-phase flow in plasma transferred arc cladding of NiCrBSi/WC metal matrix composite. Int. J. Heat Mass Transf. **232**, 125 944 (2024). https://doi.org/10.1016/j.ijheatmasstransfer.2024.125944

[15] L. Wang, T. Zhou, Z. Zhang, Y. Guo, and X. Xia, Simulation on directional dispersion of WC parti cles in laser dispersion process based on heat-fluid-structure coupling. Heat Treat. Met. **51**(1), 309–3 16 (2026). http://www.jsrcl.net/EN/Y2026/V51/I1/309

[16] P.K. Kundu, I.M. Cohen, and D.R. Dowling, Fluid Mechanics, 5th ed., Amsterdam, Academic Press, 2016.

[17] Y. Jiang, Y. Cheng, X. Zhang, J. Yang, X. Yang, and Z. Cheng, Simulation and experimental invest igations on the effect of Marangoni convection on thermal field during laser cladding process. Optik, **203**, 164044 (2022). https://doi.org/10.1016/j.ijleo.2019.164044

[18] L. Chen, T. Yu, P. Xu, and B. Zhang, In-situ NbC reinforced Fe-based coating by laser cladding: Si mulation and experiment. Surf. Coat. Technol. **412**, 127027 (2021). https://doi.org/10.1016/J.SURFCO AT.2021.127027

[19] J. Gao, S. Tian, C. Yuan, Z. Ma, C. Gao, G. Yan, R. Li, Q. Tan, and L. Zhang, Design and optim ization of a novel double-layer Helmholtz coil for wirelessly powering a capsule robot. IEEE Trans. Power Electron., **39**(1), 1826–1839 (2024). https://doi.org/10.1109/TPEL.2023.3321845

[20] Z. Long, Y. Hu, X. Duan, X. Li, L. Yin, Y. Chen, and J. Xie, Formation mechanism of waveform interface in Mg/Al electromagnetic pulse welding. Mater. Today Commun. **45**, 112401 (2025). https://doi.org/10.1016/J.MTCOMM.2025.112401

[21] C.T. Crowe, M. Sommerfeld, and Y. Tsuji, Multiphase Flows with Droplets and Particles, 2nd ed., Boca Raton, CRC Press, 2011.

[22] L. Schiller, Uber die grundlegenden berechnungen bei der schwerkraftaufbereitung. Z. Vereines Detsc her Ingen. **77**, 318 (1933).

[23] C. Ancalmo and S.P. Narra, Prediction of the powder catchment efficiency and melt track height in laser directed energy deposition. J. Manuf. Process. **137**, 207–220 (2026). https://doi.org/10.1016/j.jmapro.2025.01.039

[24] C. Li, H. Sun, X. Han, W. Ge, and Y. Sun, Study on the performance of laser cladding Ni-based WC60 composite coatings. J. Adhes. Sci. Technol. **39**(9), 1395–1426 (2025). https://doi.org/10.1080/01694243.2025.2450267

[25] C. Li, T. Jia, X. Han, and X. Jiang, Study on parameter optimization of laser cladding Fe60 based on GA-BP neural network. J. Adhes. Sci. Technol. **37**(18), 2556–2586 (2023). https://doi.org/10.1080/01694243.2022.2159298

[26] J. Gao, C. Wu, Y. Hao, X. Xu, and L. Guo, Numerical simulation and experimental investigation on three-dimensional modelling of single-track geometry and temperature evolution by laser cladding. Opt. Laser Technol. **129**, 106287 (2020). https://doi.org/10.1016/j.optlastec.2020.106287

[27] X. Han, C. Li, X. Chen, and S. Jia, Numerical simulation and experimental study on the composite process of submerged arc cladding and laser cladding. Surf. Coat. Technol. **439**, 128432. (2022). https://doi.org/10.1016/J.SURFCOAT.2022.128432